Ignition/Duct Overpressure Induced by Space Shuttle Solid Rocket Motor Ignition

Hideo Ikawa* and Fred S. Laspesa†
Rockwell International, Downey, California

An analytical methodology, with a propagating solid rocket motor (SRM) exhaust front as a perturbation pressure wave generator, is developed to enhance understanding of the ignition/duct overpressure (IOP/DOP) induced during the Space Shuttle liftoff. Waveform, amplitude, and low-frequency responses of IOP/DOP are simulated. For a full-scale configuration, IOP and DOP responses are clearly isolated and distinguishable. However, in the subscale tests, an interaction region of IOP and DOP exists, which obscures interpretation of the test data. The methodology offers a first-order assessment of these phenomena with respect to the launch complex geometry and the SRM ignition transient, and provides guidance for the test data interpretation.

Nomenclature

a = speed of sound of gas
a^* = maximum speed of sound of exhaust $\sqrt{2\gamma R T_{cm}/(\gamma+1)}$
A = point of IOP/DOP convergence
C = speed of sound of air
D_i = longitudinal instrument locations on duct ceiling, $i=1,2,3$
f = wave function, $f(t-r/C)$
$h_{\text{duct}}, W_{\text{duct}}, X_{\text{duct}}$ = duct coordinates with respect to DOP convergence point
K, K_f = multiplying factors, Eqs. (4) and (8), respectively
L = characteristics length, Eq. (4)
m_j = $1+0.5\ (\gamma-1)M_j^2$
M_j = exhaust jet Mach number
M_{wj} = wall-jet Mach number
MLP = mobile launch platform
p_4 = perturbation pressure in region 4, Fig. 1
$\bar{p}$ = $(p_4/p_{02})^{(\gamma-1)/\gamma}$
p_c = plenum chamber pressure
p_{cm} = maximum plenum chamber pressure
$\bar{p}_c$ = p_c/p_{cm}
p_e = ambient pressure
p_{02} = stagnation pressure in region 2, Fig. 1
p^* = $(2/\gamma)\ (p_{cm}/p_e)^{(\gamma-1)/\gamma}$
r = height above launch platform or DOP source
R = gas constant
t = time from ignition
T_c = plenum chamber temperature
T_{cm} = maximum plenum chamber temperature
$\bar{T}_c$ = T_c/T_{cm}
u_j = exhaust jet velocity
u_k = $0.5\gamma(\gamma+1)(u_p/a_e)^2$, Eq. (11)
u_p = velocity of piston or contact surface
u_s = propagating wave velocity in region 4, Fig. 1
u_{wj} = wall-jet velocity
v_c = convection velocity, Eq. (12)
V_{wind} = wind velocity
x,y,z = duct coordinates
x_d = vertical distance from nozzle exit to flame deflector
x_u = vertical distance from flame deflector to duct opening
X_D = longitudinal distance of duct ceiling
z_c = centerline of wall-jet
α = $\arccos[-(x-x_0)/\sqrt{r^2+(x-x_0)^2+z_c^2}]$
γ = ratio of specific heat of air or gas
Δ = wall-jet thickness or incremental change
η = $t-(r/C)\sec\theta, t-(r/C)\sqrt{1+\tan^2\theta+\tan^2\psi}$
θ = $\arctan[(z-z_0)/r]$
ν = Prandtl-Meyer angle
τ = delayed time
ψ = $\arctan[(x-x_0)/r]$

Subscripts

e = ambient condition
j = exhaust plume
L = left limit of duct
R = right limit of duct
0 = coordinate origin of convergence point
4 = properties in region 4, Fig. 1

Introduction

DURING the first launching of the Space Shuttle from the Eastern Test Range (ETR), the launch vehicle experienced the propagations of a strongly impulsive compression wave. This wave was induced by the ignition transient of the solid rocket motor (SRM) and was emanating from the large SRM duct openings on the mobile launch platform (MLP). This phenomenon is called ignition overpressure (IOP). Subsequent study indicated that IOP will impact the dynamic responses of vehicles and payloads.

To develop an effective IOP suppression system, an extensive subscale testing (6.4% scale model with Tomahawk SRM) was conducted at the Marshall Space Flight Center (MSFC) with the cooperation of all NASA centers and Space Shuttle contractors. The finalized IOP suppression system consists of water trough covers across the duct openings to provide the physical barrier and water injections into the SRM exhaust to quench the thermal energy. This combined system reduced the IOP phenomenon effectively for the STS-2 (Space Transportation System, flight 2) and the subsequent STS launchings.[1,2]

Presented as Paper 83-1113 at the AIAA/SAE/ASME 19th Joint Propulsion Conference, Seattle, Wash., June 27-29, 1983; received Sept. 12, 1983; revision received June 6, 1984.

*Member of Technical Staff. Member AIAA.

†Supervisor, STS Airload Evaluation.

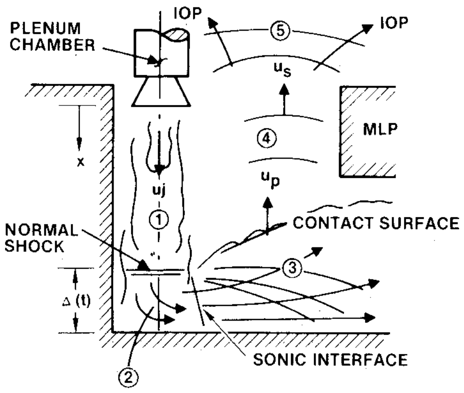

1. EXHAUST JET, $u_j = u_j(\dot{p}_c)$
2. IMPINGEMENT ZONE (SUBSONIC FLOW) $p_{t2} = p_{t2}(\dot{p}_c, \Delta\tau 2)$
3. WALL JET REGION (SUPERSONIC STREAM) $u_p = u_p(\dot{p}_{t2}, \Delta\tau 2)$ ACCELERATING — DECELERATING CONTACT SURFACE
4. COMPRESSION-RAREFACTION WAVE PROPAGATING REGION $u_S = u_S(u_p, \Delta\tau 4)$
5. EXTERNAL IOP PROPAGATION REGION

REGIONS 3 AND 4 ARE REPRESENTED BY SHOCK TUBE ANALOGY

Fig. 1 SRM IOP model.

The Western Test Range (WTR) launch complex, under development, has a completely enclosed exhaust duct configuration as compared to the open configuration of the ETR. Therefore, it was anticipated that the IOP environment at the WTR might be greater. However, screening test results of the subscale model with the water injection IOP suppression system indicated that the primary IOP was found to be approximately the same low level as that of the STS-2 and subsequent. However, a new concern is the appearance of dominant duct overpressure (DOP) emanating from the downstream exits of the exhaust ducts.

The Space Shuttle IOP phenomenon is unique because the exhaust duct configuration has two large cut-outs on the launch platform which allow the induced pressure to escape. The flowfields of both IOP and DOP are highly complex and are not well understood. For example, a numerical analysis of the plume transient in a simplified duct model requires several hours of computation.[3,4] However, it provides only qualitative behaviors of the internal flow mechanism without offering the external vehicle environment. The present analytical methodology represents one of the many hypotheses which have been postulated.[1,5-8] However, relatively accurate predictions of this phenomenon give some credence to this methodology. The computation is rapid and suitable for engineering analysis. The model also identifies that IOP response is sensitive to the duct geometry and the transient characteristics of the SRM. Hence, the scaling parameters for interpreting the subscale model test data with relation to the full-scale vehicle must consider the differences in ignition transient between the Tomahawk and the Space Shuttle SRM's.

IOP Mathematical Model

A summary description of the IOP prediction model is presented herein because the detailed derivation of the IOP prediction is discussed in Ref. 5. The strength of the propagating wave is most pronounced in the azimuthal direction in which the wave-generating front propagates.[9] Therefore, the main theme of this model is given as the upward propagating pressure wave, with sufficient strength along the vertical vehicle, must be generated in the same upward direction. To satisfy this requirement, the mechanism for a primary wave generator is postulated as the thickness growth rate of the wall-jet, produced by the impinging exhaust plume at the bottom of the duct.

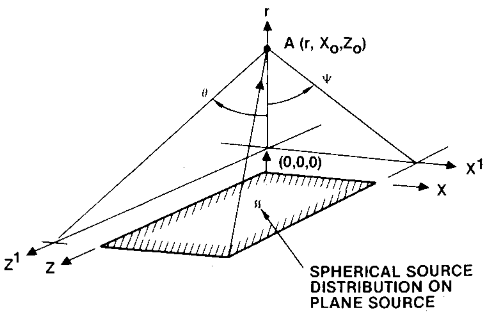

Fig. 2 External wave propagation model.

The schematic of the IOP model is shown in Fig. 1. The original hypothesis which led to the development of the transient exhaust plume column is based on the study of the high-speed movie film taken during the demonstration firing of the Space Shuttle SRM (DM-3). The film indicated that the visible plume developed in radial and longitudinal directions with respect to the transient ignition history. The plume column development is assumed to follow an isentropic process in the nozzle, downstream of the throat. Hence, the jet Mach number with the plume core varies with respect to the p_c history. The deceleration of plume flow by the entrainment process is neglected during the rapid ignition transient (region 1).

The rate of change of jet velocity is given by

$$\frac{\mathrm{d}u_j}{\mathrm{d}t} = 0.5a^*\sqrt{\bar{T}_c(\gamma+1)M_j^2/2m_j}\left[\frac{\mathrm{d}\ell_n T_c}{\mathrm{d}t} + \left(\frac{1}{m_j}\right)\frac{\mathrm{d}\ell_n M_j^2}{\mathrm{d}t}\right] \tag{1}$$

and the rate of change of Mach number, which is proportional to the rate of change of p_c is

$$\frac{\mathrm{d}M_j^2}{\mathrm{d}t} = p^*\bar{p}_c^{(\gamma-1)/\gamma}(1/\bar{p}_c)\frac{\mathrm{d}p_c}{\mathrm{d}t} \tag{2}$$

The subsonic region behind the normal shock (region 2) is determined by the Rankine-Hugoniot relation. The wall-jet grows in size as the mass flux increases. As the stagnation pressure in the wall-jet increases proportional to the p_c history, the wall-jet becomes supersonic and the boundary expands with the Prandtl-Meyer process until the pressure continuity is satisfied (region 3). The rate of change of the Prandtl-Meyer expansion fan is given by

$$\frac{\mathrm{d}\nu}{\mathrm{d}t} = [\sqrt{\bar{p}(\gamma-1)[2-\bar{p}(\gamma+1)]/2\gamma(1-\bar{p})}]$$
$$\times[1-\gamma(M_j^2-1)^2p^*p_c^{(\gamma-1)/\gamma}/M_j^2m_j(2\gamma M_j^2-\gamma+1)]\frac{\mathrm{d}\ell_n p_c}{\mathrm{d}\tau} \tag{3}$$

The displacement velocity of the wall-jet boundary is taken as the piston velocity of the shock tube analogy to generate the perturbation pressure pulse. It is approximated as

$$u_p = \frac{\mathrm{d}\Delta}{\mathrm{d}\tau} + KL\frac{\mathrm{d}\nu}{\mathrm{d}\tau} \tag{4}$$

The piston response characteristic is proportional to the rise rate of the SRM plenum chamber pressure ($p_c$dot [Eqs. (3) and (4)]. Regions 1 and 4 are assumed to be isolated with no first-order interaction occurring. The compression wave perturbation is given by

$$p_4/p_e - 1 = 0.5[u_k + \sqrt{u_k^2 + 8\gamma u_k/(\gamma+1)}] \tag{5}$$

The expansion wave perturbation is given by

$$p_4'/p_4 = [1-0.5(\gamma-1)(u_4-u_p)/a_4]^{2\gamma/(\gamma-1)} \tag{6}$$

where $u_p < u_4$; u_4 and p_4 are defined for passage of the last compression wave preceding the deceleration of the piston (contact surface).

The time delay for the arrival of the perturbation pressure wave at the opening of the duct is defined as

$$(\tau_4)_i = t_i + (x_d/u_j)_i + (x_u/u_s)_i \tag{7}$$

where (i) is at the ith event.

The external pressure wave propagation is computed by the three-dimensional acoustic theory (Fig. 2).[5] The perturbation pressure waves emerge from the rectangular-shaped SRM duct cut-out on the MLP. Therefore, the amplitude decaying follows a cylindrical wave solution $(1/\sqrt{r})$ at near field and a spherical wave attenuation $(1/r)$ at far field. Transitional behaviors exist at the intermediate point. The following solution satisfies the required conditions

$$p(t,r,x_0,z_0)/p_e$$

$$= \frac{K_f}{C}\int_{\psi_0}^{\psi}\left\{\int_{\eta_L}^{\eta R}\frac{(\Delta p(\eta)/p_e)'_{r=0}\,\mathrm{d}\eta}{\sqrt{(t-\eta)^2-(r/C)^2\sec^2\psi}}\right\} r\sec^2\psi\,\mathrm{d}\psi \tag{8}$$

Note that a forcing function $(\Delta p(\eta)/p_e)'$ is proportional to the second derivative of the transient pressure history (p_c double-dot); hence, an externally traveling wave has an N-wave response.

The computed and the measured pressure waves are shown in Fig. 3. The zero time reference is biased for the comparison. The waveform and frequency response are well simulated. The amplitudes are different because the point of computation is taken on the Orbiter side fuselage near the payload bay and the measurement is on the Orbiter base heat shield, where the maximum IOP was recorded.

DOP Analytical Model

During the WTR 6.4% scale model IOP tests, low-frequency overpressures were found dominant for the WTR launch environment. The wave arrival time followed after the SRB ignition transient (Fig. 4), indicating an indirect path of wave travel exists. Subsequently, the wave was determined to be emanating from the downstream exit of the SRM exhaust duct. Re-evaluation of the ETR data reveals that this phenomenon also exists, but its presence is obscured by the dominant IOP. However, analytical prediction based on a single-point wave generator is unable to simulate the low-frequency responses and the delayed wave arrival time.

In order to simulate the observed phenomenon, a propagating SRM exhaust front (a wall-jet in the horizontal duct) must be considered as the moving wave generator. The present model is formulated in accordance with the schematic representation of duct flow model as given in Fig. 5.

The analytical model includes the following approximations and assumptions:

1) The strength of compression waves in the duct is proportional to:

Transient exhaust mass flux, which follows p_c history.

Rate of change of stagnation pressure history at the bottom of the duct.

Thickness growth rate, which is proportional to the rate of change of the Prandtl-Meyer fan [Eq. (3)].

Wall-jet retardation by wall friction, which is neglected at this time (it may become an important mechanism).

Three-dimensional spreading of the impinging exhaust plume, which was approximated by a multiplying factor proportional to a square root of area ratio between plume cross section and duct opening.

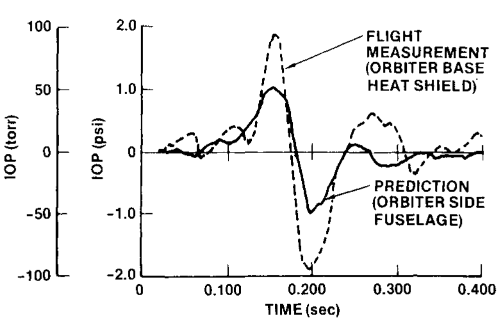

Fig. 3 IOP comparison: STS-1 flight measurement and prediction (zero time reference is biased for comparison).

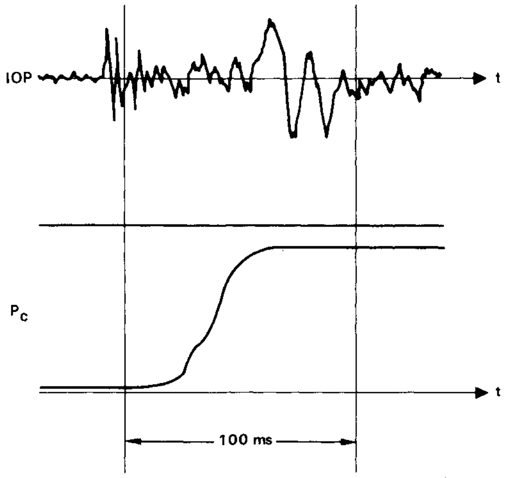

Fig. 4 WTR subscale test: p_c and DOP timing relation.

2) The internal DOP, which converges on a point on the duct ceiling, is determined by the following:

Summation of pressure pulses (Fig. 6) is performed by the same integral [Eq. (8)] used for the external wave analysis, except that wave propagation speed C is replaced by $v_c = C + u_{\mathrm{wj}}\cos\alpha$ to produce a frequency shift effect. $u_{\mathrm{wj}}\cos\alpha$ is a converging velocity component of local convective exhaust front and a) $\cos\alpha > 0$ for a perturbation flow upstream of a point, and b) $\cos\alpha < 0$ for a perturbation flow downstream of a point.

The pressure sources are uniformly distributed laterally across at a fixed longitudinal point on the duct floor.

The strengths of sources are nonuniformly distributed in a longitudinal direction on the duct floor.

3) The external overpressure responses on the vehicle and the surrounding structures are determined by three-dimensional acoustic wave propagation theory [Eq. (8), Fig. 2].

The strength of a forcing function is the internal DOP solution of the duct ceiling analyzed at the downstream exit.

The crosswind effect is simulated by modifying the propagation speed C by $C + V_{\mathrm{wind}}$.

Since the fundamental solution of the externally propagating DOP depends on the accuracy of the internal flow mechanism, the duct flow model is hypothesized on the basis of pressure measurements taken under the MLP during the STS-3 flight and on the duct ceiling during the WTR subscale tests. However, the analytical model does not include the water injection effect. Therefore, an attempt is made to capture only the salient feature of this complex phenomenon; no effort is made to achieve an exact simulation.

The wall-jet velocity is expressed by the stagnation pressure history behind the normal shock as the exhaust impinges upon the flame deflector (region 2, Fig. 1). Since the mass flux does not initially fill the duct floor, the exhaust spreading effect

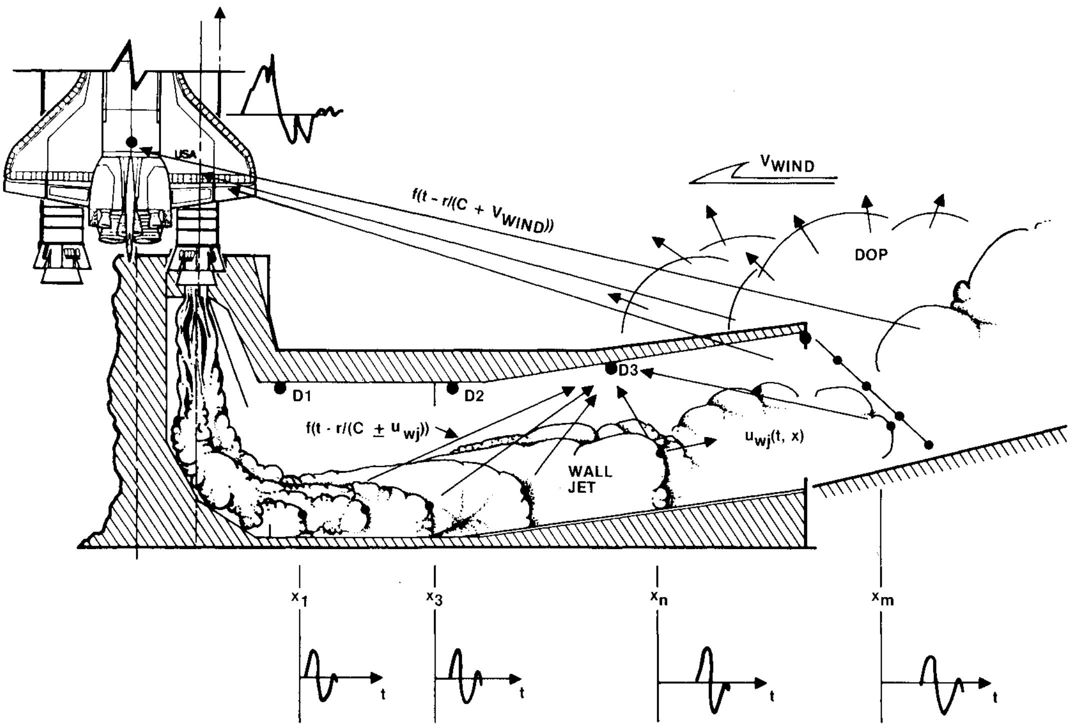

Fig. 5 SRM DOP model.

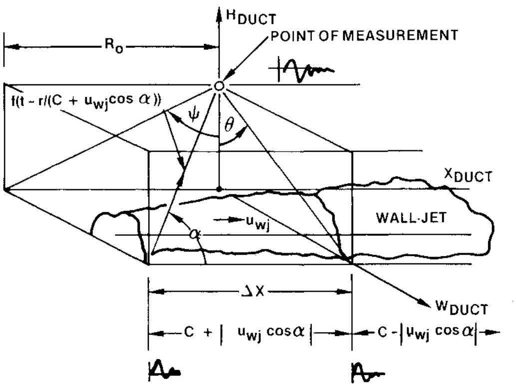

Fig. 6 Integration scheme for internal DOP response.

retards the propagating wall-jet front. Therefore, the strength of the wall-jet front is empirically corrected proportional to the mass flux (i.e., p_c history).

The wall-jet Mach number is expressed as

$$M_{wj} = \bar{p}_c\sqrt{2[(p_{02}/p_e)^{(\gamma-1)/\gamma} - 1]/(\gamma-1)} \tag{9}$$

and the wall-jet velocity as

$$u_{wj} = M_{wj}\, a_j \tag{10}$$

where a_j can be determined by the duct temperature. For simplicity without loss of generality, a_j is assumed to vary linearly from the value of the vertical plume at the beginning of the duct to the ambient value at the downstream exit. The water mixing is expected to alter this property which may influence the strength of the DOP-generating mechanism.

Another factor, a development of convective wall-jet thickness, contributes to the generation of a pressure pulse at a given longitudinal position. Hence, a multiplying factor proportional to the rate of change of the Prandtl-Meyer fan normalized by its maximum value [(Eq. (3)] is used to correct the source strength further.

$$u_k = 0.5\gamma(\gamma+1)\left(\frac{u_{wj}}{a_j}\right)^2\left[\frac{(\mathrm{d}\nu/\mathrm{d}\tau)}{(\mathrm{d}\nu/\mathrm{d}\tau)_{\max}}\right] \tag{11}$$

Then, this quantity is substituted into Eq. (4) to compute the local pressure pulse histories over the wall-jet boundary.

The pressure waves converge from the wall-jet boundary to the duct ceiling in the same manner as the external wave propagates. The integration scheme is shown in Fig. 6. The strengths of the distributed source term in Eq. (8) are determined by the derivative of pressure pulse, which is proportional to the p_c double-dot ($\ddot{p}_c$).

The velocity of a traveling wave, which replaces the term C in Eq. (8), is expressed by

$$v_c = C + u_{wj}\cos\alpha \tag{12}$$

When $v_c < 0$, the perturbation source is outside the domain of influence; hence, the signal cannot reach a point of interest. Once the strength of the DOP source at the duct exit is determined, the external wave propagation is computed by the same integral used for the IOP problem [Eq. (8)].

In this methodology, the prediction requires the input data consisting of 1) the physical dimensions of the launch complex geometry, 2) the position where the IOP/DOP prediction is desired, and 3) the actually measured plenum pressure histories of the SRM. The p_c history is normally digitized and the p_c-dot history is self-generated by numerical differentiation. However, this technique produces spurious spikes and it is necessary to truncate these spikes to a reasonable quantity.

Another technique is to smooth the numerically differentiated data first, then the smoothed p_c-dot history is digitized to be used as the input data. Subsequent numerical integration reproduces the p_c history.

Discussion of Results

The external IOP/DOP predictions for the ETR and the WTR are made on an Orbiter lower surface (Orbiter stations in inches: $x = 1285$, $y = -6$, $z = 260$) where the flight and the model test instrumentations are located. For the 6.4% subscale model test, the measured p_c history of the Tomahawk SRM's are used. Unfortunately, the repeatability of each SRM characteristic is inconsistent. For the full-scale configuration, the measured p_c-history of the STS-1 SRM is used. The transient behaviors of all Space Shuttle SRM's are found consistently repeatable. The pertinent p_c histories are shown

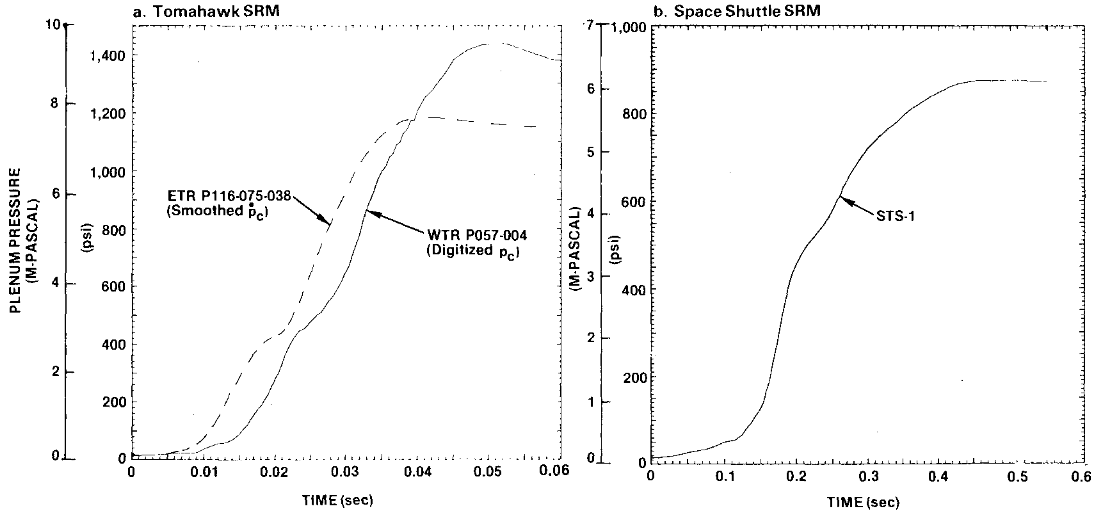

Fig. 7 Tomahawk and Space Shuttle SRM p_c histories.

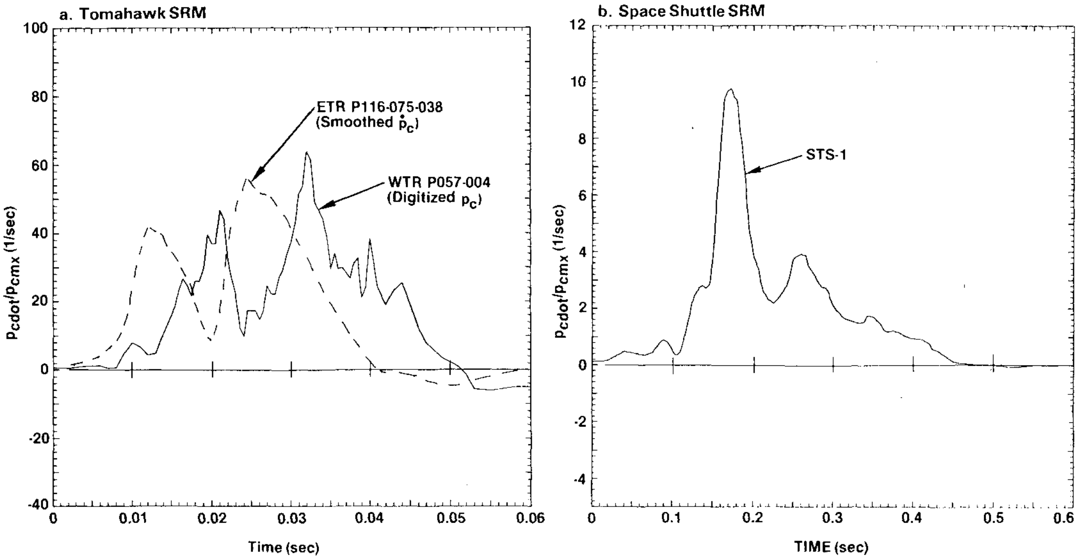

Fig. 8 Tomahawk and Space Shuttle SRM p_c-dot histories.

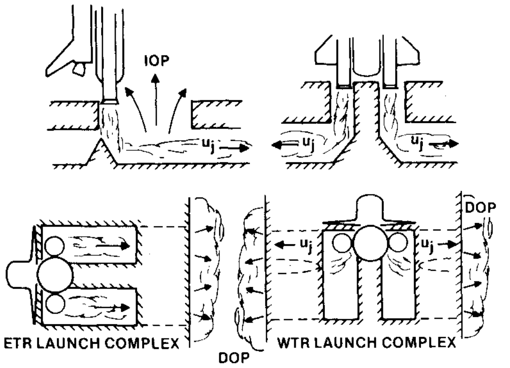

Fig. 9 ETR and WTR launch complex geometries.

in Fig. 7. The corresponding p_c-dot histories are shown in Fig. 8. The Tomahawk SRM data are represented by two input techniques, i.e., by digitizing the p_c history (WTR test P057-004) and by digitizing the p_c-dot history (ETR test P116-075-038). The general characteristics of the two data are identical, if the zero time references are biased, except for the spikes appearing in the WTR data (Fig. 8a). The smoothness of the p_c-dot history does reflect the qualitative response of the predicted IOP/DOP.

The primary difference between these SRM's is the characteristic of the second p_c-dot peaks. For the Space Shuttle SRM, the first p_c rise rate predominates (Fig. 8b) and is expected to produce a single N-shape wave. However, for the Tomahawk SRM, the second p_c rise rate is found to be equal to or greater than the first (Fig. 8a); hence, a double response wave is expected for the subscale tests.

Schematic sketches that depict the difference in duct configurations between the ETR and the WTR are shown in Fig. 9. For the ETR, the position of the flame deflector directs the impinging exhaust, the primary IOP generator, toward the open area of a large rectangular cut-out on the MLP, from where most of the IOP escapes. However, the flame deflector for the WTR is shaped so that it forces the exhaust to flow directly under the covered tunnel immediately upon the impingement, as confirmed by the heat-imprinted flow pattern. Therefore, a little amount of IOP generating wall-jet propagates in the direction of the opening. If the present hypothesis represents the correct IOP mechanism, then the flame deflector configuration is partially responsible in suppressing the WTR IOP observed in the subscale tests.

The qualitative behaviors of typical internal pressure responses, computed at three equally spaced longitudinal stations on the duct ceilings, is shown in Fig. 10 (solid lines). The development of the internal wave structures can be ob-

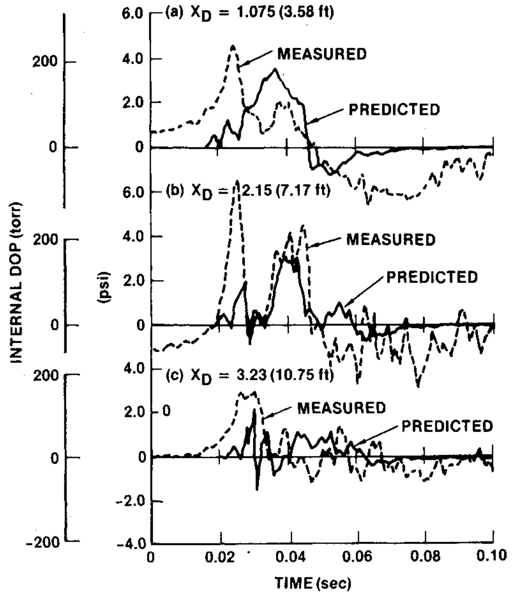

Fig. 10 Comparison of internal DOP on the duct ceiling: WTR 6.4% scale test.

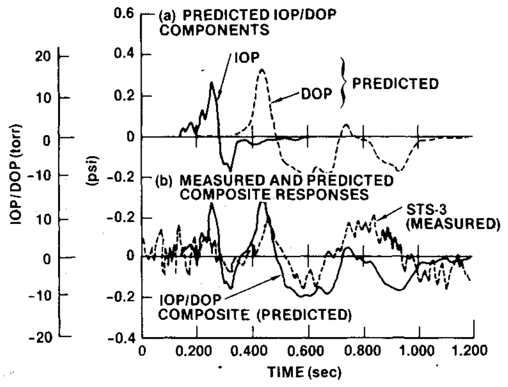

Fig. 11 Comparison of STS-3 full-scale external IOP/DOP histories.

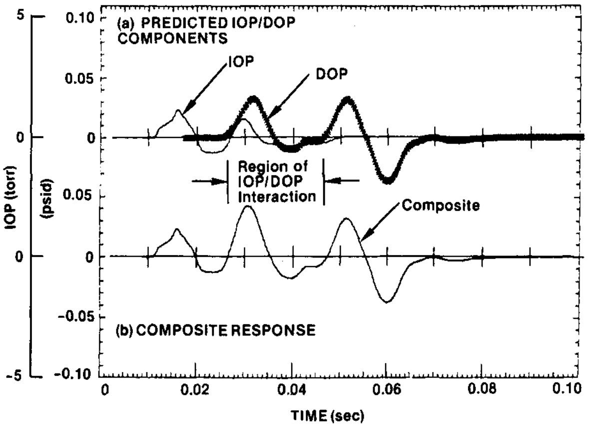

Fig. 12 Computed STS-3 subscale external IOP/DOP histories.

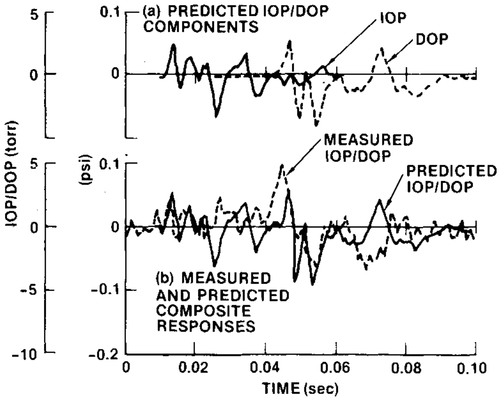

Fig. 13 Comparison of WTR subscale IOP/DOP histories.

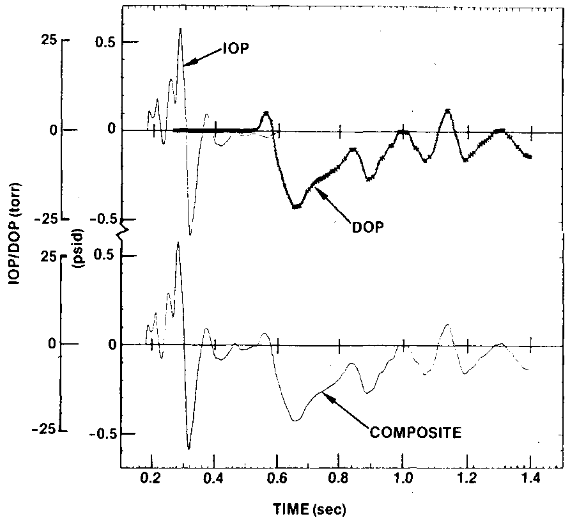

Fig. 14 Computed WTR full-scale IOP/DOP histories.

served in the downstream direction. The initially large-scale wave pattern at the beginning of the duct (Fig. 10a) is developed into a smaller pattern at the downstream stations (Fig. 10c) by superposition of high-frequency components produced by the interaction of many converging waves. The typical measurements (dashed lines), taken during the WTR subscale tests, show the similar pattern development qualitatively at approximately the same computed locations. The water injection effects, not simulated in the prediction, may be partially responsible for the observed qualitative differences.

The external waveforms for the STS-3 are shown in Fig. 11. The DOP and IOP are computed independently (Fig. 11a) and a composite response is constructed by a linear superposition of both data (solid line, Fig. 11b). The measured data (dashed line) are overlaid on Fig. 11b. Although the details are not simulated exactly, the salient features of the phenomenon are captured and favorably compared.

The IOP/DOP predictions of the subscale model test for the STS-3 launch are shown in Fig. 12, and for the WTR in Fig. 13. Although both configurations have displayed an interaction region of IOP and DOP, the WTR data show a greater separation because the duct is almost twice as long as the ETR configuration. Two factors, the acoustic speed of propagating waves in the ambient media and the exhaust speed of the SRM, cannot be scaled geometrically in the subscale model tests. They are within the same order of magnitude for the full-scale and subscale conditions. Yet, the model test configuration is an order of magnitude smaller (1/16). Therefore, a region of IOP/DOP interaction can be produced for the subscale configuration. The problem is amplified because the second peak of the Tomahawk SRM is more pronounced; hence, an IOP wave of the second peak and a DOP wave of the first peak may arrive simultaneously on a vehicle to produce a complex pressure interaction (Fig. 12).

The measured WTR subscale test data, overlaid on Fig. 13b (dashed line), compares favorably with the prediction. However, no simple method of wave separation is available to identify the independent contributions of IOP and DOP. Hence, the analytical methodology becomes the important tool in order to understand the test data.

The prediction of IOP/DOP histories for the full-scale WTR is given in Fig. 14. The IOP and DOP are clearly separated and easily distinguishable. The waveform responses of the DOP for both ETR and WTR are qualitatively different (Figs. 11 and 14). Since the same SRM p_c history and Orbiter location were used for both predictions, the apparent difference is attributable to the duct configuration change. As shown in Fig. 9, the WTR SRM exhaust ducts are located at the opposing positions. This may pose a problem if a wind blows in a direction from the one duct exit to the opposite side and/or two SRM ignitions are mismatched. The perturbation pressure waves emanating from both of the duct exits will be convected by the wind, and the wave arrival time upon the launch vehicle will be shifted. For example, a wind velocity of 15.24 m/s (50 ft/s) in a direction from the left to the right ducts produces approximately 10-15 ms of mismatch in wave arrivals, as observed in Fig. 15. Consequently, it induces undesirable yaw force loadings which may impact the payload.

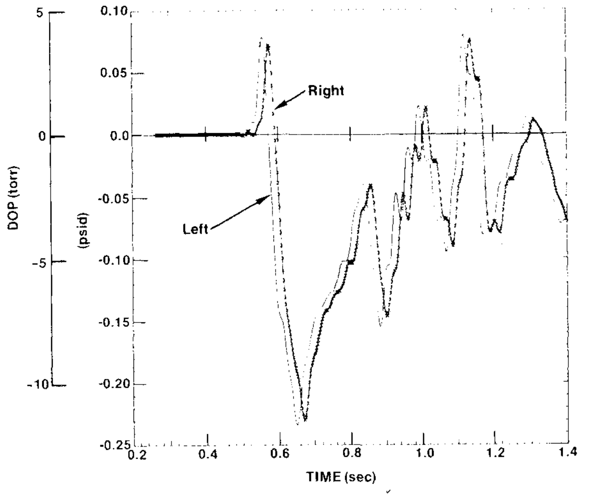

Fig. 15 Computed WTR full-scale DOP histories of right and left ducts (wind effects on wave arrival time; wind velocity of 15 m/s from left to right).

The full-scale internal DOP developments, computed on the duct ceiling at every quarter length point, are compared for the ETR and the WTR configurations (Fig. 16). Although the periods of initial response for both are almost identical, the period of response taken near the exit (Fig. 16f) is greater for the WTR than the one for the ETR (Fig. 16c). The pattern is also more complex because a longer duct length induces more complicated interactions.

Conclusion

An analytical methodology that offers some physical understanding of the IOP/DOP mechanism has been developed. Reasonably good correlation of prediction and test data gives credence to this methodology. The methodology offers rapid engineering solutions with respect to launch complex geometry and rocket motor ignition transient for this complex phenomenon.

Since the strength of the DOP generating mechanism appears to be related to the velocity of the convective wall-jet front, the DOP strength may be reduced by the wall-jet retardation mechanism. The primary IOP for the WTR is believed to be partially reduced by the orientation of the flame deflector, which directs the exhaust flow under the covered tunnel immediately upon plume impingement. The ceiling of the tunnel provides the physical barrier for the wave escape, as did the water trough for the ETR. Interaction of water and plume, which removes thermal energy, also is believed to have caused the IOP attenuation. However, the water and plume may have mixed more effectively at the bottom of the duct where a pool of water has accumulated prior to the ignition.

Acknowledgment

This methodology has been developed under company-sponsored independent research and development (IR&D).

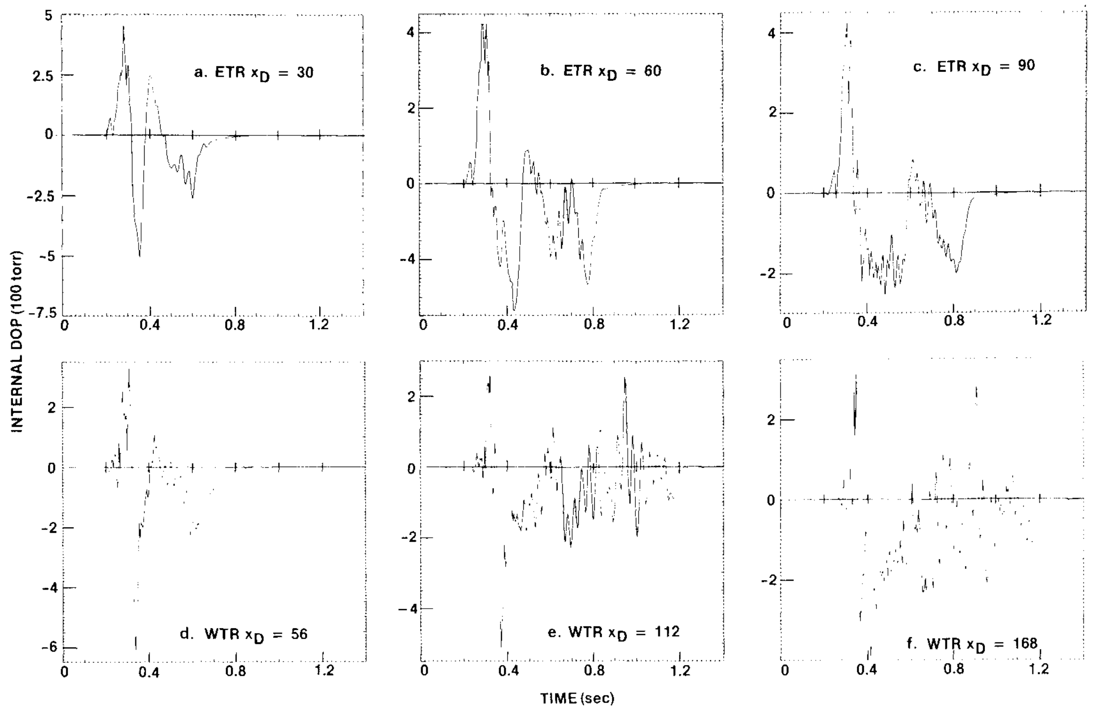

Fig. 16 Full-scale internal DOP development: ETR/WTR comparisons.

References

[1] Lai, S. and Laspesa, F.S., "Ignition Overpressure Measured on STS Lift-off and Correlation with Subscale Model Tests," *JANNAF 13th Plume Technology Meeting,* CPIA Pub. 357, April 1982, pp. 207-216.

[2] Dougherty, N.S., Nesman, T.E., and Guest, S.H., "Shuttle SRB Ignition Overpressure: Model Suppression Test Program and Flight Results," *JANNAF 13th Plume Technology Meeting,* CPIA Pub. 357, April 1982, pp. 217-244.

[3] Rapagnani, N.L. and Lutton, R.J., "Study of the Overpressure Effect on STS Launch," IOP Working Group Meeting, April 1982.

[4] Wilmoth, R.G. and Cline, M.C., "Numerical Simulation of Shuttle SRB Ignition Overpressure," IOP Working Group Meeting, April 1982.

[5] Ikawa, H. and Laspesa, F.S., "Space Shuttle Solid Rocket Motor Ignition Overpressure Prediction Methodology," *JANNAF 13th Plume Technology Meeting,* CPIA Pub. 357, April 1982, pp. 245-256.

[6] Li, C.P., "Simulation of Solid Rocket Startup Transient Flow Using a Numerical Method," *JANNAF 13th Plume Technology Meeting,* CPIA Pub. 357, April 1982, pp. 359-370.

[7] Simon, E.D., "Ignition Overpressure Correlation for Titan III 7.5-percent Model and Flight Data," *JANNAF 13th Plume Technology Meeting,* CPIA Pub. 357, April 1982, pp. 359-370.

[8] Jones, J.H., "Scaling of Ignition Startup Pressure Transients in Rocket Systems as Applied to the Space Shuttle Overpressure Phenomenon," *JANNAF 13th Plume Technology Meeting,* CPIA Pub. 357, April 1982, pp. 371-392.

[9] Fansler, K.S. and Schmidt, E.M., "A Model of the Blast Overpressure Caused by Transient Exhaust Plume," *JANNAF 13th Plume Technology Meeting,* CPIA Pub. 357, April 1982, pp. 331-342.

From the AIAA Progress in Astronautics and Aeronautics Series...

ENTRY VEHICLE HEATING AND THERMAL PROTECTION SYSTEMS: SPACE SHUTTLE, SOLAR STARPROBE, JUPITER GALILEO PROBE—v. 85

SPACECRAFT THERMAL CONTROL, DESIGN, AND OPERATION—v. 86

Edited by Paul E. Bauer, McDonnell Douglas Astronautics Company
and Howard E. Collicott, The Boeing Company

The thermal management of a spacecraft or high-speed atmospheric entry vehicle—including communications satellites, planetary probes, high-speed aircraft, etc.—within the tight limits of volume and weight allowed in such vehicles, calls for advanced knowledge of heat transfer under unusual conditions and for clever design solutions from a thermal standpoint. These requirements drive the development engineer ever more deeply into areas of physical science not ordinarily considered a part of conventional heat-transfer engineering. This emphasis on physical science has given rise to the name, thermophysics, to describe this engineering field. Included in the two volumes are such topics as thermal radiation from various kinds of surfaces, conduction of heat in complex materials, heating due to high-speed compressible boundary layers, the detailed behavior of solid contact interfaces from a heat-transfer standpoint, and many other unconventional topics. These volumes are recommended not only to the practicing heat-transfer engineer but to the physical scientist who might be concerned with the basic properties of gases and materials.

Volume 85—Published in 1983, 556 pp., 6×9, illus., $35.00 Mem., $55.00 List
Volume 86—Published in 1983, 345 pp., 6×9, illus., $35.00 Mem., $55.00 List

TO ORDER WRITE: Publications Order Dept., AIAA, 1633 Broadway, New York, N.Y. 10019